LIMNOLOGY and OCEANOGRAPHY: METHODS

ASLO

Limnol. Oceanogr.: Methods 23, 2025, 26–38

doi: 10.1002/lom3.10660

A membrane inlet laser spectrometer for in situ measurement of triple water isotopologues

Axel Wohleber,* **Camille Blouzon, Julien Witwicky, Patrick Ginot, Nicolas C. Jourdain, Roberto Grilli***
Université Grenoble-Alpes, CNRS, IRD, Grenoble INP, INRAE, IGE, Grenoble, France

Abstract

We describe a novel compact autonomous in situ sensor for semi-continuous measurement of water isotopes (δD, $\delta^{18}O$, and $\delta^{17}O$) in liquid water. The sensor relies on a dual-inlet water vapor injection system based on the pervaporation through a semi-permeable membrane, and on the water vapor composition analysis using a dedicated optical feedback cavity enhanced absorption spectrometer. The sensor has dimensions of 165 mm diameter and 550 mm long, for a weight of ∼ 8 kg. A titanium casing allows applications down to 6000 m deep for a total effective weight of 45 (23) kg in air (water). It has a power consumption of ∼ 40 W, and an autonomy of 10–12 h which is ensured by a dedicated Li-ion battery pack. The sensor is equipped with single-pair high-speed digital subscriber line communication for telemetry purposes. The instrument provides an accuracy of 0.3‰ (2σ) for all water isotopes with a 9-min integration time. The instrument is suitable for investigating the freshwater cycle in the ocean, and in particular the transformation of ocean water masses related to iceberg and ice shelf melting.

The polar oceans play a critical role in the global climate system, acting as a heat (Swart et al. 2018) and a carbon sink (Gruber et al. 2019). The melting of land ice in the ocean, in the form of icebergs and ice shelves, significantly changes the properties of water masses, and thereby affects the global thermohaline circulation and the global climate (Serreze and Barry 2011; Golledge et al. 2019; Schloesser et al. 2019). Changes in ice shelf melting by the ocean also threaten the ice shelf stability in Antarctica and North Greenland (Pritchard et al. 2012; Millan et al. 2023). Given that ice shelves buttress the ice sheet and keep it stable, this could accelerate the ice sheet contribution to sea level rise (Dupont and Alley 2005). Over the past decades, both the Arctic and Antarctic regions have experienced important changes in temperatures and salinities, which influences its climatic roles (Haumann et al. 2016; Polyakov et al. 2017; Sallée et al. 2021; Akhoudas et al. 2023). However, the processes that explain these changes remain elusive because ocean properties are influenced by multiple processes, including precipitation–evaporation, sea-ice formation, and land-ice melting (Carter et al. 2008).

Due to this complexity, a simple measure of temperature and salinity is not sufficient to understand the origin of a given seawater volume. Noble gases, such as helium or neon, may provide additional information on the water origin as ice shelf water can be supersaturated in noble gases due to the dissolution of air entrapped in continental ice (Schlosser 1986). The isotopic composition of seawater is also a useful tracer of water masses, containing finger-print information on their formation condition, transport, and evolution (Friedman 1953; Craig and Gordon 1965). The isotopic signal may be highly decoupled from salinity and temperature, allowing a better discrimination of the different sources. Sea-ice meltwater or brine rejection during its formation strongly influence seawater salinity with little changes in isotopic composition. In contrast, high-latitude precipitations are strongly depleted in heavy isotopologues and therefore has a considerable impact on the isotopic signature of the water mass (Frew et al. 2000). Stable isotopologues of water are also a valuable tool for analyzing hydrological processes and studying their impact on and sensitivity to climate changes. As heavy and light isotopes pass through phase changes at different rates, due to variations in atomic mass and diffusion rates (Dansgaard 1964),

*Correspondence: axel.wohleber@univ-grenoble-alpes.fr; roberto.grilli@cnrs.fr

Author contribution statement: Conceptualization: RG, NJ; Data curation: AW, CB, JW, PG, RG; Formal analysis: AW, CB, RG; Funding acquisition: RG, NJ; Investigation: AW, CB, JW, RG; Methodology: AW, CB, JW, RG; Project administration: RG; Visualization: AW, CB, RG; Writing of the original draft: AW, CB, RG; Revision of the article: AW, CB, JW, PG, NJ, RG.

Additional Supporting Information may be found in the online version of this article.

their proportion in water bodies reflects a history of exchanges between different hydrological reservoirs (Gat 1996; Galewsky et al. 2016). As a result, the measurement of water isotopes provides an additional proxy for analyzing the hydroclimatic system, providing information that goes beyond more conventional hydrological measurements.

When studying ocean water masses, the stable isotopologues of water generally considered are $H_2{}^{16}O$, $H_2{}^{18}O$, $H_2{}^{17}O$, and $HD^{16}O$ (from the most to the least abundant). The isotopic ration R_x is calculated from the concentration $[X]$ of a given isotopologue as:

$$R_X = \frac{[X]}{k[H_2{}^{16}O]} \quad (1)$$

where $H_2{}^{16}O$ is the concentration of the most abundant water isotopologue and k is a factor of 1 for $H_2{}^{18}O$, $H_2{}^{17}O$ and of 2 for $HD^{16}O$, indicating the number of atoms in the molecule that can be substituted.

Isotopic measurements must be metrologically referenced with respect to a standard material in order to compare isotopic composition. The isotopic ratio is compared to a reference water composed of a mixture of distilled waters from oceanic waters collected in different points of the globe (Vienna standard mean ocean water [VSMOW]) (Nelson 2000). The difference with respect to the VSMOW standard is called isotopic deviation (δ) and described by Eq. 2, where R_X is the isotopic ratio of a specific isotopologue in the sample, and $R_{X(VSMOW)}$ is the isotopic ratio of these same isotopologue in the reference:

$$\delta X(‰) = \left(\frac{R_X}{R_{X(VSMOW)}} - 1\right) \times 1000 \quad (2)$$

The use of isotopic deviation permits the measurements to be referenced and compared within different instruments and techniques. This allows to remove possible systematic errors while providing absolute isotopic deviation measurements. [Correction added on December 6, 2024, after initial online publication: In Equation 2, the "x" has been capitalized in two occurrence; also in the text part "RVSMOW' has been replaced with "RX(VSMOW)" in this version.]

Currently, the variability of isotopes of water or noble gases in the ocean remains scarcely documented because of the difficulty of making precise mapping of isotopic ratio in water masses. Both measurements are conducted by laboratory analysis of discrete water samples using Niskin bottles or similar sampling systems (Akhoudas et al. 2020). This method is time-consuming and limited in spatial and temporal resolution due to its discrete nature. Monitoring the isotopic ratios at higher spatial and temporal resolution—as it is currently possible for temperature and salinity—would allow a better characterization of the water mass transformations around Antarctica. Tides, for example, have been reported as important drivers of ice-shelf basal melting at diurnal and semi-diurnal frequencies (Padman et al. 2018), so there is a major interest for obtaining measurements at the process time scales.

To measure stable water isotopes, different methods exist, such as isotope ratio mass spectroscopy (IRMS) (Walker et al. 2016) or absorption spectroscopic methods using optical resonators or multi-pass cells (Dyroff et al. 2010; Walker et al. 2016). The determination of the isotopic composition by IRMS method is bulky, expensive, and time-consuming (therefore only adapted to laboratory analysis), while optical spectroscopy techniques reach similar performances while being more compact, less expensive, and easier to use (Kerstel 2004; Walker et al. 2016).

Laser spectrometers have been developed to measure water isotopes by direct absorption using multipass cells for near-infrared at 1400 nm (Kerstel et al. 2002; Gianfrani et al. 2003) and in the mid-infrared at 2660 nm (Dyroff et al. 2010). This technique is not suitable in our case. Achieving sufficient optical path lengths, between 50 and 100 m, is necessary to measure $H_2{}^{16}O$, $H_2{}^{18}O$, $H_2{}^{17}O$ and $HD^{16}O$. However, the required cavity geometries result in a large cell volume, which is less adapted for an in situ sensor. A larger cell volume increases the internal surface area, leading to longer flushing times and a bigger memory effect. It also requires handling a larger water vapor volume, which poses challenges for the pumping system, increases the consumption of the water used as a reference standard, and complicates the storage and trapping of water vapor inside the instrument. In addition, the instrument would be less compact and less suitable for certain types of deployment, such as through boreholes: the larger is the instrument diameter, the longer and more difficult and energy demanding is the hot-water drilling. The hole is then closing back within a certain time, and having a small measurement will give more chance of deployment. To reduce the volume of the measurement cell and the dimensions of the instrument, it is possible to use techniques based on resonant cavities. Developments using these resonant cavities have been made with the off-axis integrated cavity output spectroscopy technique at 6700 nm (Sayres et al. 2009) with a 90-cm-long cavity cell and precision on δD and $\delta^{18}O$ of 50‰ and 30‰ for 5 ppmv of water; optical-feedback cavity-enhanced absorption spectroscopy (OF-CEAS) (Kerstel et al. 2006) at 1400 nm with a lightweight (45 kg) and small (< 50 liters) instrument for a final precision in stratospheric condition of 1‰, 3‰, and 9‰ for $\delta^{18}O$, $\delta^{17}O$, and δD; and by cavity ring-down spectroscopy (Brand et al. 2009) at 1400 nm for a final precision of 0.04‰ and 0.2‰ for $\delta^{18}O$ and δD, but with an instrument whose dimensions are not compatible for an in situ embedded spectrometer.

The OF-CEAS (Morville et al. 2014) used in this work is a reliable, robust, and widely used technique for trace gas detection (Richard et al. 2018). OF-CEAS has already been used to monitor the isotopic composition of water vapor in the atmosphere (Landsberg et al. 2014) from airborne (Kerstel et al. 2006), study exhaled gas in the health sector (Ventrillard-Courtillot et al. 2009), vapor continuum measurement (Lechevallier et al. 2018; Fleurbaey et al. 2022), and

embedded in field deployed instruments for measuring the dissolved gas composition (Grilli et al. 2018). In this work, we coupled this spectrometer to a dual-inlet pervaporation system using polydimethylsiloxane (PDMS) membranes allowing the generation of a sample and reference water vapor mixture. The compact in situ instrument presented in this work can offer different types of deployment: from a vessel, going through a borehole for vertical variability beneath the ice shelf or embedded in autonomous or remote underwater vehicles for water isotope cartography. It reached an accuracy of 0.3‰ (2σ) on referenced measurements of $\delta^{18}O$, δD, and $\delta^{17}O$ within 9 min, providing a reasonable temporal resolution with more than six datapoints per hour.

Materials and methods

The optical spectrometer

The Subsea Water Isotopic Sensor (SWIS) instrument described in Fig. 1 is based on the OF-CEAS technique which takes advantage of the fact that the radiation spectrally filtered by the optical cavity is allowed to get back to the laser, narrowing down its emission and reducing the phase noise. For the optical feedback (OF), to work correctly, the phase of the photon getting back to the laser needs to match the one of the photons emitted by the laser. For this, one of the two steering mirrors of the optical path is mounted on a piezoelectric transducer (PZT) which adjusts in real-time the laser-to-cavity distance (Morville et al. 2005). During a frequency scan, the laser emission is locked on the successive narrow cavity resonances, which improves the laser/cavity coupling and therefore the signal intensity at the output of the resonator. This makes the OF-CEAS technique highly sensitive in terms of absorption, as the light interacts over longer optical path length. On the frequency axis, the optical resonator provides a well-defined grid, with each point separated by the cavity's free spectral range (FSR).

A distributed feedback laser diode from Nanoplus centered at 1967 nm wavelength is focused by an aspheric lens (C036TME-D, $f = 4$ mm, Thorlabs) in the middle of a 20-cm-long mono-block aluminum V-shape cavity. A near-infrared polarizer (Color-Por) was used in order to add losses (in a controlled manner) of the photons coming back to the polarized

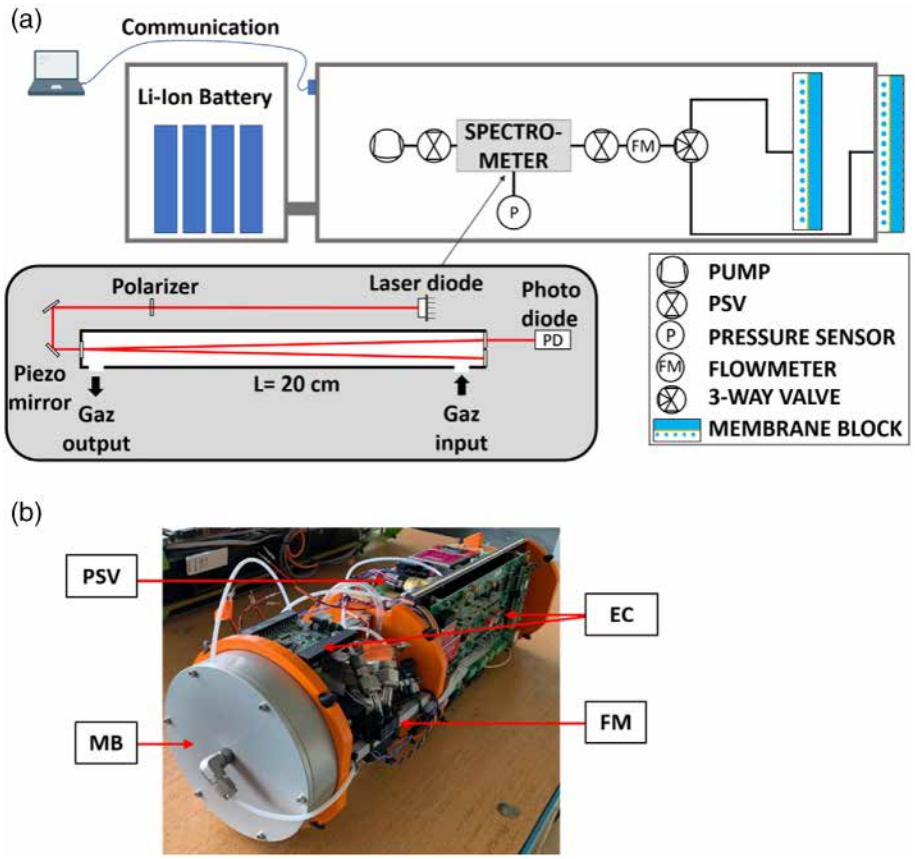

Fig. 1. (**a**) Schematic and (**b**) picture of the SWIS instrument. The water vapor flow to be analyzed comes from the two membrane blocks (*see* "The membrane inlet laser spectroscopy technique" section) with two different waters: the in situ sample water and the reference water for standardizing the measurement and comparing it with other measurements. These blocks pervaporate the liquid water, which is then sent through the optical spectrometer. The three-way valve allows to switch between the two samples. EC, electronic cards; FM, flowmeter.

laser. This would change the feedback rate (photons returning to the laser with respect to the photons emitted by) therefore changing the strength of the OF. Two aluminum steering mirrors (PF05-03-G01, $R > 95\%$, Thorlabs) are used for injecting the laser into the high-finesse cavity. The cavity is composed by three high-reflectivity mirrors ($R > 99.99\%$ and $T \sim 0.0015\%$ at 1965 nm, Layertec, 154458). A near-infrared photodiode (G12183, Hamamatsu) with a bandpass of 1 MHz is used to acquire the signal at the cavity output. The wavelength scan is performed by ramping the current of the laser diode, while stabilizing its temperature. The output signal shows successive broad cavity modes when the optimal feedback rate is set, with the laser frequency emission staying locked during each cavity resonance. Each mode would provide one spectral element; therefore, the spectral resolution is dictated by the cavity geometry: the smaller the cavity is, the more spectrally spaced the resonant modes are. The FSR of a 20-cm-long V-shaped cavity is 375 MHz, which is 1.3 times the full-width-half-maximum of the sampled absorption water lines at 8 mbar of gas pressure, which translates into approximatively three datapoints per line. An electronic card from the company AP2E is used to control all the components of the spectrometer.

The gas handling

The measurement cell has an internal volume of $< 10\ cm^3$ and internal surfaces are treated with silcolloy to reduce surface interactions of water molecules and protect against corrosion. The cell is thermally stabilized at 35°C by a heating band and a proportional integral derivative (PID) controller based on the reading of a PT1000 (457-3603, RS PRO) probe placed at the center of the optical cavity and glued to the aluminum block. The cell is then isolated using 5-mm-thick cork sheet. To retrieve the absorption profile, and thus the intra-cavity molecular density with a relative error in the range of 0.1‰, the cavity must be stabilized in temperature with precision better than $\pm$ 0.1°C.

The pressure is controlled by dynamically adjusting the flow rate of the gas sample using a vacuum pump (SVF-2, Scroll Labs) and two proportional solenoid valves (PSVs) (PVQ31, SMC). The PSV at the cavity inlet is used to restrain the flow rate in order to reach low pressure with the dedicated vacuum pump. The PSV at the cavity outlet is controlled by a PID algorithm based on the reading of the pressure in the cavity by a 0–50 mbar absolute pressure gauge (ATM.1ST, STS) to dynamically adjust and stabilize the pressure inside the cavity. The PID is set to 8 mbar to ensure a sufficient pressure drop at the dry side of the membrane for pervaporating the water vapor for a wide range of water temperatures (*see* "Characterization of water vapor permeation at the PDMS membrane" section). Pressure stabilization from unregulated to steady-state takes $\sim$ 40 s, with a standard deviation of $\sim$ 0.003 mbar for steady-state regulation. The water vapor flow is measured at the cavity outlet by using a 0–50 standard cubic centimeters per minute (sccm) flowmeter (HAFBLF0050CAAX5, Honeywell).

The mechanical housing, autonomy, and communication

The instrument fits in a homemade titanium pressure casing made of a 700-mm-long tube of 190 mm outside diameter (165 mm of inside diameter). Two 45-mm-thick titanium flanges close the housing and ensure the sealing. One flange is designed for holding the measurement membrane and the other for hosting the electric connectors for communication and power supply. A 120-mm diameter 10-μm-thick PDMS membrane (Contros) is mounted on a 3-mm-thick 120-mm diameter stainless-steel porous disk. The pressure housing was designed to withstand a hydrostatic pressure of 600 bars.

The sensor is powered with 24V DC and it has a power consumption of $\sim$ 40 W during operation. For autonomous deployment, it is equipped with four Li-ion batteries in parallel (WILPA2749A 6S1P, Williamson Electronique) with a total capacity of 30 Ah and an autonomy of 10–12 h of deployment depending on external temperature. The batteries are packaged in a 285-mm-long titanium casing with the same diameter of the instruments.

The instrument weight is about 8 kg, with a final weight of 45 kg in the titanium casing (final buoyancy in water $\sim$ 23 kg), while battery pack weights 5 kg (20 kg with the titanium casing and final buoyancy of $\sim$ 12 kg).

The instrument has an embedded PC (conga-PA5 Pico-ITX SBC, Congatec) allowing to be fully autonomous during operation. Communication with the instrument can be achieved by single-pair high-speed digital subscriber line (SHDSL) two-wire communication protocol (Lantiq Sacrates SHDSL card, Wurth Electronik).

A table summarizing all the components of the spectrometer is provided in the Supporting Information Section S1.

The spectral region and fit

To perform high-precision isotopic ratio measurements with the OF-CEAS technique, the absorption lines should have an intensity on the order of $10^{-6}\ cm^{-1}$. This order of intensity allows to use the full dynamic range of the technique and therefore an optimum signal-to-noise ratio on the acquired spectra. At higher absorption levels, the OF at the top of the absorption lines decreases, leading to narrow and weak resonance modes which compromise the precision in the retrieved peak surfaces. Additionally, high absorption results in a nonlinear signal intensity. According to those criteria, the wavelength region around 1967 nm was selected, allowing simultaneous measurement of $H_2{}^{16}O$, $H_2{}^{18}O$, $H_2{}^{17}O$, and $HD^{16}O$ (Table 1). The absorption lines are sufficiently separated from each other (Fig. 2a). Regarding other possible interferents, there is a CO_2 line at 1967.64 nm, but it is well isolated from the water lines and is also very low in intensity because there is no water renewal at the membrane. This

Table 1. List of spectral lines of water isotopologues in the spectral region 1967.50–1967.75 nm with the most intense spectral line of carbon dioxide.

Isotopologue	Wavelength (nm)	Line intensity (cm^{-1} $molec^{-1}$ cm^{-2})	Einstein coefficient (s^{-1})	Lower-state energy (cm^{-1})	Line temperature dependency (‰ K^{-1})
$H_2{}^{18}O$	1967.531	1.49×10^{-25}	0.2016	282	−3.78
$H_2{}^{18}O$	1967.547	3.97×10^{-27}	18.82	2384	29.8
$H_2{}^{17}O$	1967.582	1.28×10^{-26}	9.122	1521	13.9
$H_2{}^{18}O$	1967.613	6.19×10^{-26}	0.08823	414	−2.16
12_C16_{O2}	1967.637	2.54×10^{-25}	0.2713	1966	21.9
$H_2{}^{16}O$	1967.672	7.71×10^{-27}	0.03045	2129	25.2
$H_2{}^{16}O$	1967.687	3.82×10^{-26}	15.2	2983	40.8
$HD^{16}O$	1967.720	1.83×10^{-25}	0.6589	304	−3.59
$H_2{}^{17}O$	1967.742	3.85×10^{-26}	9.133	1521	14.1

causes a rapid depletion of dissolved gases at the membrane boundary layer, resulting in an inefficient gas extraction.

To determine the concentration of each species in the spectrum, the absorption lines are fitted with a Rautian line shape using a multicomponent fit routine, and each parameter is adjusted to obtain the lowest fit residual. For this purpose, five parameters were defined from a simulation with the HITRAN 2016 database (Gordon et al. 2017) and adjusted according to the spectrum: the intensity and relative position of the absorption lines as well as their broadenings; the Lorentzian related to the collisions of the molecules, the Gaussian related to the Doppler effect and the Dicke narrowing coefficient related to the reduction in the width of the spectral line due to collisions in the gas. In order to reduce the computation time, and thus to allow the spectrum to be fitted in real time, all those parameters are fixed. They are optimized for a given gas temperature and pressure by adjusting each value line by line for achieving the smallest possible standard deviation on the fit residual. For this purpose, an interlaced spectrum was used to obtain a higher spectral resolution and thus be able to optimize the parameters. It is obtained by slowly sweeping the cavity temperature over 0.05°C temperature range, which results in a shift in the position of the cavity modes (with respect to the absorption features), as a consequence of mechanical deformation of the cell by thermal effect. The spectra obtained during the scan are then combined and homogeneously distributed across the one FSR interval to create the interlaced spectrum. An example of interlaced spectrum is shown in Fig. 2b. This spectrum, represented by the blue dots, has a 10 times higher resolution than the conventional spectrum, reported with white squares.

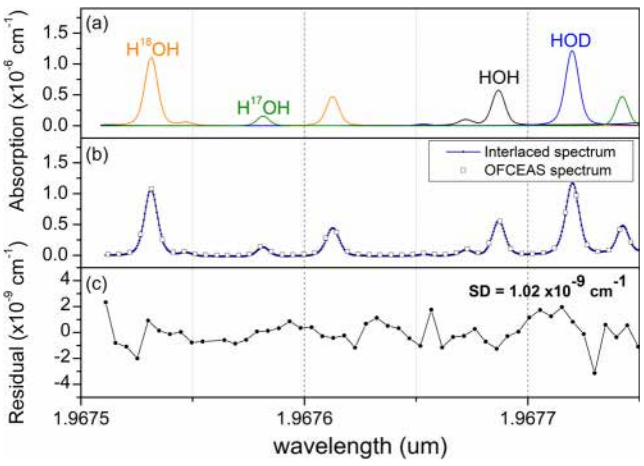

Fig. 2. (**a**) Simulation of an absorption spectrum of pure water vapor at 35°C and 8 mbar using the HITRAN 2016 database. (**b**) Example of an interlaced spectrum (blue line with blue dots) used to improve the fit, whose resolution is 10 times higher than a single OF-CEAS spectrum (white squares). (**c**) Residual of the fit on a single OF-CEAS acquisition (160 ms).

The following parameters are left free: (1) the mode shift corresponding to the global position of the cavity modes with respect to the position of the absorption spectrum; (2) the intensities of $H_2{}^{16}O$, $H_2{}^{18}O$, $HD^{16}O$, and $H_2{}^{17}O$ absorption lines allowing to determine the concentration of each of these four molecules. The relative intensity of multiple lines of the same species are grouped together based on the theoretical intensity ratios between these lines and fitted with a single parameter; (3) the three polynomial coefficients of the 2nd-order polynomial function for drawing the fit baseline.

Figure 2a shows a simulation of the spectrum by the HITRAN 2016 database for a temperature of 35°C and a pressure of 8 mbar for each absorbing molecule in the selected spectral region. In order to have a more realistic simulation and to consider the continuum absorption coming from nearby strong absorbing lines, we widened the spectral region by 5 at the time of making the simulation. The experimental spectrum (blue line and square dots in Fig. 2b) is in good agreement with the spectral simulation. The spectral fit leads to a standard deviation of the residual of 1.02×10^{-9} cm^{-1} (Fig. 2c). This result corresponds to a sensitivity of ~ 1‰ for the three isotopes δD, $\delta^{18}O$, and $\delta^{17}O$ within a single acquisition spectrum (160 ms) for a sample of pure water vapor.

The membrane inlet laser spectroscopy technique

In situ underwater optical spectroscopy is performed by vaporizing liquid and introducing it into the low-pressure optical cavity. The sampling method chosen here, pervaporation through a permeable membrane, is used for more than 60 yr (Hoch and Kok 1963). It is well adapted with the constraints of in situ measurements because it does not require any sample preparation. The permeation allows to vaporize liquid and introduce either dissolved gas and/or water vapor into the spectrometer through a selective permeable membrane. This method, coupled with an optical spectrometer, allows the analysis of dissolved gas concentrations (Grilli et al. 2018), their isotopic signature (Grilli et al. 2022), as well as the isotopic composition of water masses as also been proposed in Downing et al. (2016) but on site rather than in situ.

Membrane inlet laser spectroscopy (MILS) uses a membrane to vaporize the water sample and act as a tight barrier between the liquid water and the instrument. These membranes are made of a silicon polymer, PDMS or polytetrafluoroethylene (PTFE), for example, with a thickness ranging from few μm to few hundreds of μm (Johnson et al. 2000). PDMS and PTFE are hydrophobic, but allows gases and water vapor pass through them (Bian et al. 2021). In our case, PDMS material was selected because of its mechanical properties when exposed to high hydrostatic pressure and has a higher water vapor permeation coefficient than PTFE. It has been shown that the pressure response of membranes follows a hysteresis phenomenon depending on whether the pressure at the membrane increases or decreases due to defects in the elasticity of the material (Bell et al. 2007). This phenomenon makes the oscillation phase of the PID pressure regulation longer, but once the cavity is well stabilized, it no longer affects it.

When a liquid sample is in contact with a permeable membrane, the molecule of water vapor is adsorbed at the membrane surface, diffuse through it, and desorb downstream the membrane. This process is driven by a difference in partial pressure of the target species. To describe this physical phenomenon, the solution-diffusion model proposed for pervaporation is used (Wijmans and Baker 1995). In agreement with Fick's 1st law, this model gives a simple expression linking the particle flux passing through the membrane and the partial pressures of each component:

$$J_i = \frac{P_i^{\mathrm{G}}}{l}\left(p_i^{\mathrm{liq}} - p_i^{\mathrm{vap}}\right) \tag{3}$$

with J_i (g s^{-1} m^{-2}) the flux of compound i through the membrane, P_i^{G}(barrer) the permeability of the membrane for the gaseous compound i, l (m) the thickness of the membrane, p_i^{liq}(Pa) and p_i^{vap}(Pa) the partial pressure for compound i in the liquid and vapor side of the membrane, respectively. For a given temperature, the partial pressure at the liquid side is equal to the saturation vapor pressure P_{sat}. The total flux passing through the membrane is $J = \sum_i J_i$.

Thus, the flow through the membrane depends on the membrane's geometry (size and thickness), the composition of the fluid on the liquid side and finally the partial pressure difference of the component in the vapor and in the liquid. Here, the partial pressure in the liquid corresponds to the saturation vapor pressure (Eq. 4). At a given temperature, it is described by the Clausius–Clapeyron equation assuming that the vapor behaves like an ideal gas and that the enthalpy of vaporization is independent of the temperature. The partial pressure of the water is directly linked to the temperature, which would therefore dictate the achievable total flow of water vapor through the membrane for a given partial pressure at the vapor side.

$$P_{\mathrm{sat}}(T) = P_0 \exp\left(\frac{\Delta H_{\mathrm{vap}}}{R}\left(\frac{1}{T_0} - \frac{1}{T}\right)\right) \tag{4}$$

with P_{sat} the saturation vapor pressure, ΔH_{vap} the enthalpy of vaporization, P_0 and T_0 the reference boiling pressure and temperature, and R the ideal gas constant.

Results and performance

Characterization of water vapor permeation at the PDMS membrane

The 10-μm-thick PDMS membranes used in this study were characterized as a function of the water temperature and the pressure behind the membrane. Figure 3 shows the dependency of the measured water vapor flow permeating the membrane. The results show that there is a linear relationship between the flow rate (or flux) and the pressure on the vapor

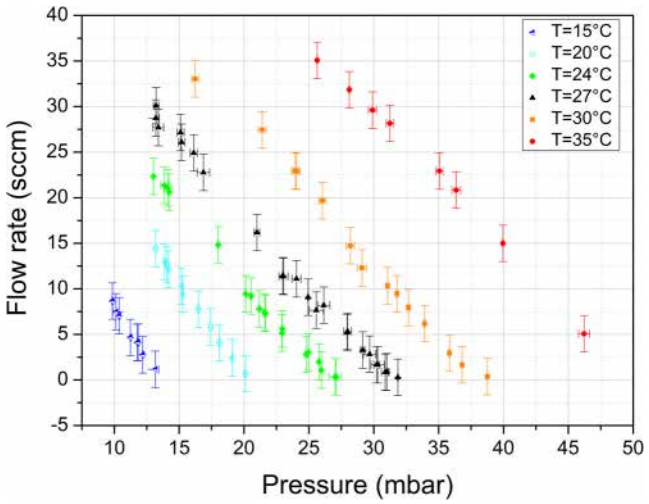

Fig. 3. Characterization of the flow of water vapor pervaporating a 10-μm-thick PDMS membrane as a function of the pressure applied downstream of the membrane and the temperature of the water. The error bars represent the standard deviation calculated over several thousands of measurement points and the systematic error due to sensor drift.

side of the membrane, as shown in Eq. 3. We also note that, as indicated by Eq. 3, the flow rate cancels out when $p_i^{liq} = p_i^{vap}$, that is, when the pressure on the vapor side reaches the saturation vapor pressure at the given temperature. So, to measure in cold water close to 5°C, a vapor pressure of less than 9 mbar must be reached. For lower temperatures, the cavity pressure must be reduced to 6 mbar at 0 °C. The impact of temperature, described in Eq. 4, is also visible in Fig. 3: for a given pressure, the higher the water temperature is, the higher the flow rate will be. According to Eq. 3, increasing the membrane thickness reduces the water vapor flow produced by pervaporation. In our case, a thicker membrane would better withstand hydrostatic pressure but will result in a lower flow of water vapor through it. Therefore, the membrane thickness should be selected based on deployment depth; for a depth of 6000 m, a membrane thickness of 30–40 μm is required.

Stability of the spectrometer

Water isotope ratio measurements for $H_2{}^{18}O$ and $HD^{16}O$ require an accuracy of 0.05‰ and 0.5‰, respectively, to resolve the variability expected nearby Antarctic ice-shelves (Akhoudas et al. 2020). The signal-to-noise ratio of the spectrometer on a single absorption spectrum measurement (160 ms integration time) does not allow to reach the required sensitivity. However, if the main component of the measurement noise is white noise, the sensitivity can be improved by averaging data over time to improve the precision. In this case, the error will decrease as $1/\sqrt{N}$ where N is the number of samples considered in the average. When the principal component of the signal no longer follows a random dispersion, then increasing the integration time will no longer improve the measurement accuracy. In the OF-CEAS system used in this work, the temperature and pressure drifts and the mechanical instabilities of the optical system are the most limiting factors for the integration time. These drifts and instabilities mainly modify the shape of the absorption lines and the value of the FSR, and therefore induce cavity modes instability. Due to the complexity of the spectral fit and to the fact that the spectral resolution of a OFCEAS spectrum is dictated by the FSR of the optical cavity (in this case, at 8 mbar it corresponds to three spectral elements for defining one absorption line), these modifications can have an impact on the determination of concentrations using the spectral fit routine (Lechevallier et al. 2019). A statistical tool, the Allan–Werle standard deviation method (Werle et al. 1993) ($\sigma_{AW\text{-}SD}$), gives the sensitivity as a function of the integration time. For this method, long datasets of several hours are required to obtain a representative statistical analysis of the system. Long-term isotopic measurements for the $HD^{16}O$ (blue), $H_2{}^{18}O$ (orange), and $H_2{}^{17}O$ (green) isotopologues performed using ultrapure water at 20°C ± 0.3°C, and the results of the statistical analysis are reported in Fig. 4. The $\sigma_{AW\text{-}SD}$ plot in Fig. 4a shows that for a single 160-ms acquisition, the instrument has a detection

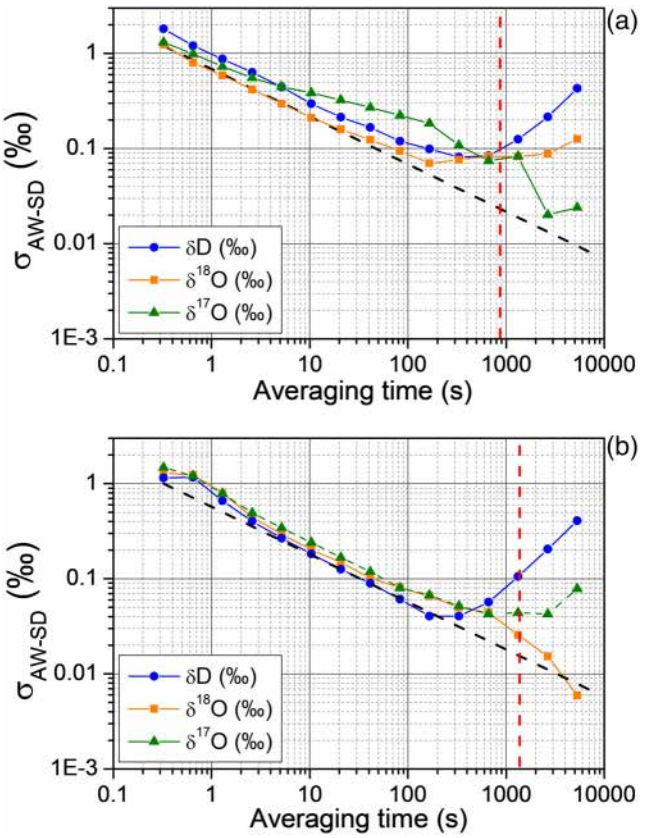

Fig. 4. (**a**) Allan standard deviation for a 4-h dataset on ultrapure water with a water vapor flow of 2 sccm. Data were obtained without stabilizing the position of the cavity modes relative to the absorption line positions. The cavity temperature was stabilized at 35°C ± 0.01°C. (**b**) Allan standard deviation for a 5-h dataset on ultrapure water at 2 sccm, with cavity mode position locking applied. The mode positions were stabilized to ± 110 kHz by adjusting the heating resistor on the cavity. The black dashed line shows the $1/\sqrt{N}$ slope representing the reduction of white noise through integration, with N as the sample count for averaging. The red dashed line marks the point at which the precisions of all isotopic signatures remain below 0.1‰.

limit of ~1‰ for the three isotopes. After 100 s of averaging, the detection limit reaches 0.1‰, 0.09‰, and 0.2‰ for δD, $\delta^{18}O$, and $\delta^{17}O$, respectively. The detection limits at the different optimum integration times for the three isotopologues are 0.08‰ at 300 s for δD, 0.07‰ at 150 s for $\delta^{18}O$ and 0.02‰ at 2600 s for $\delta^{17}O$. The sensitivity appears limited by the instabilities of the cavity modes position described before, and by possible imperfections of the fit parameters. A previously used method for fixing the position of the cavity modes consists of dynamically changing the temperature of the cavity which acts on the FSR of the resonator (Lechevallier et al. 2019). Using this method revealed a regulation of the position of the cavity modes at ±110 kHz (1σ), corresponding to 6×10^{-4} with respect to the FSR of the cavity, which is an improvement of a factor of 10 compared to the development presented by Lechevallier et al. (2019). The Allan–Werle standard

deviation of the three datasets obtained by using this method are plotted in Fig. 4b. The lock of the position of the cavity modes improves the sensitivity except for $\delta^{17}O$, and the result is more visible for the $\delta^{18}O$ signal. The significant signal enhancement for the $\delta^{18}O$ can be explained by the position of the $H_2{}^{18}O$ lines at the edge of the spectral region. If the position of the cavity modes is not stabilized, part of the peak's base may fall outside the fitted area, resulting in information loss and degraded performance. By locking the mode positions, the fit is systematically performed using the same spectral points, improving the long-term stability of the measurement. The final sensitivities are 0.04‰ in 165 s of integration for δD, 0.006‰ in 5500 s for $\delta^{18}O$ and 0.04‰ in 600 s for $\delta^{17}O$. Beyond these times, the slope of the $\sigma_{\text{AW-SD}}$ slowly rises up for δD and $\delta^{17}O$. With the locking mode method, the instrument stability time is extended from 900 to 1500 s with respect to the case without mode locking (Fig. 4b). During this time, one must measure both the reference and the measurement samples to be under 0.1‰ for the three isotopologues. The improvement in the long-term stability on the $\delta^{18}O$ due to the modes position locking is also a considerable improvement since this signature experiences a muted variability with respect to the δD signal.

Measurement protocol

The measurement protocol of the instrument is composed of three steps: (1) removing of traces of the previous sample from the cavity before each measurement, (2) stabilization of the cavity pressure and modes position, and (3) the measurement itself. The most time-consuming step is the cavity cleaning. Indeed, comparative studies between IRMS and optical analyzers have shown accuracy problems with optical spectrometer results for water isotope measurements (Penna et al. 2012) explained by a stronger memory effect of the $N-1$ measurement on the N measurement (Olsen et al. 2006). It is noted that the effect is stronger for waters with larger isotopic difference. The importance of the memory effect can then be estimated from a memory factor (Eq. 5) representing the amount of the sample $N-1$ still present in the measurement cell at a certain time:

$$x_i = \frac{\delta_{i,\text{meas}} - \delta^n}{\delta^{n-1} - \delta^n} \tag{5}$$

where $\delta_{i,\text{meas}}$ is the measured isotopic composition, δ^n is the actual isotopic composition of the sample being analyzed, and δ^{n-1} is the isotopic composition of the previous sample.

To determine the response time of the SWIS probe, laboratory tests were carried out to find the best strategy for reducing the time needed to clean the cavity. We placed two different waters with known isotopic signature in the reference and measurement membrane block (MB): −80‰ and −85‰ on the δD signature. The δD was chosen for this because the memory effect is more important on it than for $\delta^{18}O$ and $\delta^{17}O$ (Gupta et al. 2009). The cleaning is performed by fully opening both PSVs, therefore operating at minimum pressure (over the entire gas line from the cell to the MB) and at maximum water vapor flow ($f = 10$ sccm for a water temperature of 25°C). Two cleaning strategies were tested: (1) a cleaning with a constant maximum flow of water vapor of the sample to be measured (continuous cleaning); (2) several successive 2-s cleanings (1.5 s of pumping with the inlet PSV open and 0.5 s with the inlet PSV close), with the number of cleanings progressively increasing (successive cleaning). Different cycling times (0.5–20 s) as well as different duty-cycles (0.25, 0.5, and 0.75) were tested for the successive cleaning method, and the best performance was reached with the 2-s cycle described above. Figure 5 shows the dependency of the memory factor as a function of the cleaning time. For the successive cleaning, the total cleaning time was considered (i.e., 2 s per cleaning cycle). For both methods, the first points have a memory factor greater than 10%, and after 200 s of cleaning, it reaches below 0.05% with successive cleaning while it is still at 6% for continuous cleaning. The decay of the memory effect follows an exponential law with time constants of 112 and 39 s for the continuous and successive method, respectively, making the latter three times more efficient. For a difference in δD of 5‰ as in the example, a memory factor of 0.02 corresponds to our target accuracy of 0.1‰ and occurs after 100 s of cleaning. The cleaning time may be adjusted depending on the expected variability of the signal that needs to be resolved and depends on the total water vapor flow during the cleaning that would be larger for warm waters. A standard protocol is composed of 100 s of cleaning, 60 s of stabilization of pressure and cavity modes, and 120 s of spectrum acquisition, leading to a total time spent on each MB of 280 s. For a complete

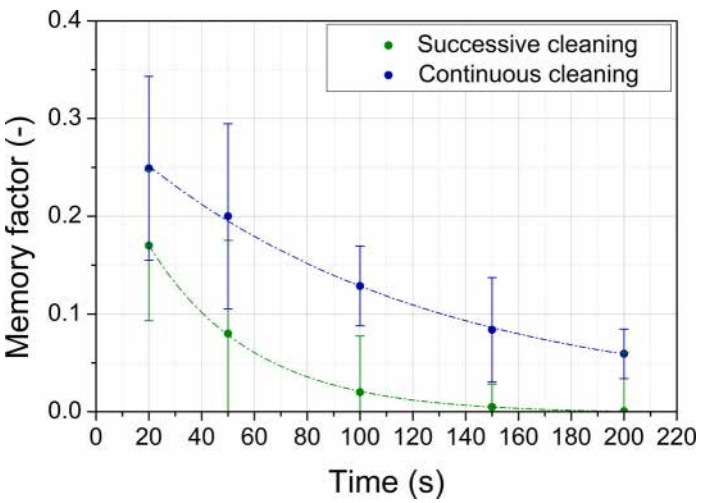

Fig. 5. Direct comparison of the memory factor for the same overall cleaning time for the successive (2-s cycles) and continuous cleaning methods. Each point was performed five times, improving the accuracy of the measurement. The MB was stabilized at 25°C.

measurement, this protocol must be carried out on both MBs, leading to a total measurement time of 560 s (~ 9 min). The time between the start of acquisition (1st spectrum acquired) on the 1st MB and the end of measurement (last spectrum acquired) on the 2nd membrane block is 380 s (~ 6 min).

The temperature dependency

The water passage through the membrane leads to a phase transition from liquid to gas which generates a mass-dependent fractionation: the lighter isotope tends to pass into the gas phase faster than the heavier isotope. This fractionation of water isotopes (i.e., $HD^{16}O$ and $H_2{}^{18}O$) changes with temperature: an increase of temperature accelerates the evaporation of the heavier isotopologues leading to an increase of the isotopic composition of the water vapor (Majoube 1971). In our case, the isotopic fractionation of water is not only dependent on evaporation but also on the way the molecules will diffuse through the membrane: due to its smaller molecular weight, the lighter isotopologue tends to diffuse through the membrane faster than the heavier isotope. To account for isotopic fractionation caused by temperature changes in the PDMS membrane, we conducted measurements in a controlled environment. We placed the measurement block in a climate chamber and the reference block in a regulated box at 20°C ± 0.1°C. The temperature in the climate chamber was set to increase by 2°C every 3 h between 8°C and 24°C. Following the analytical method described previously, we carried out measurements and obtained the evolution of the isotope measurement as a function of temperature (Fig. 6). Both $HD^{16}O$ (Fig. 6a) and $H_2{}^{18}O$ (Fig. 6b) isotopes showed a linear relationship with temperature, but with different magnitudes of 0.71‰ ± 0.02‰ °C^{-1} and 0.15‰ ± 0.04‰ °C^{-1} for δD and $\delta^{18}O$, respectively. However, the reliability of $\delta^{18}O$ measurements was lower than that of δD due to its smaller isotopic variation close to the instrument's sensitivity, resulting in a correlation coefficient R^2 of 0.57. Therefore, for reaching the required accuracies of 0.5‰ for δD and 0.5‰ for $\delta^{18}O$, water temperature must be retrieved with a precision of 0.7°C and 0.33°C, respectively, which is feasible during in situ measurements.

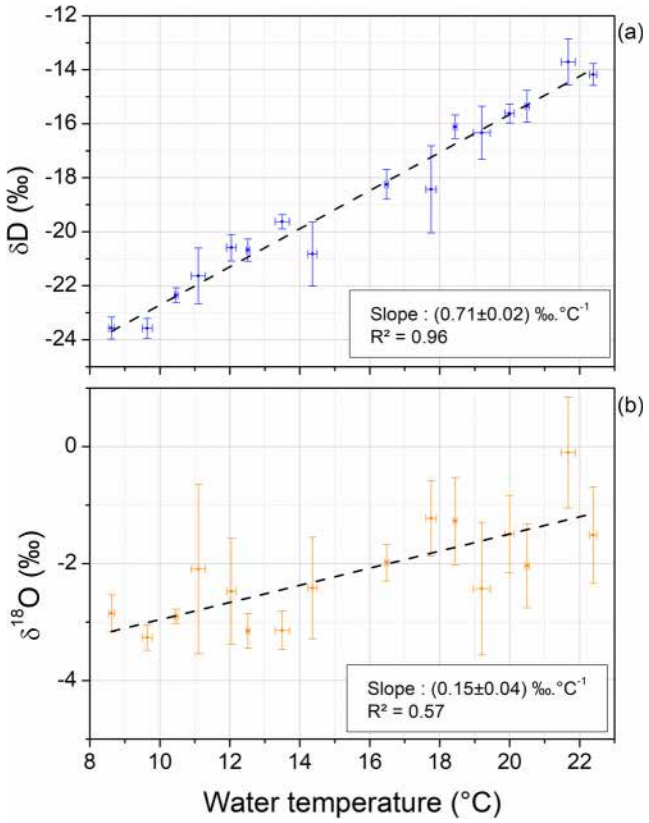

Fig. 6. Forty-eight-hour laboratory measurement of the evolution of the isotopic signatures as a function of the temperature of the measurement membrane. (**a**) Result for δD with a linear regression of slope 0.71‰ ± 0.02‰ °C^{-1} and correlation coefficient $R^2 = 0.96$. (**b**) Result for $\delta^{18}O$ with a linear regression of slope 0.15‰ ± 0.04‰ °C^{-1} and correlation coefficient $R^2 = 0.57$.

Comparison with existing instruments and results discussion

In order to prove the reliability of this novel in situ instrument and the adequacy of its measurement procedure, a laboratory intercomparison between the SWIS probe and a commercial Picarro L2140i instrument has been performed. To validate the good performance of the instruments, a relatively wide isotopic range of the samples was selected. The sample preparation and a list of the measured samples with the expected isotopic values are reported in the Supporting Information Section S2. The measurements were conducted in the following days within the same week and at the same laboratory temperatures for both instruments (21°C). The measurement procedure as well as the way the data were processed is detailed in the Supporting Information Sections S3.1 and S4.1. The isotopic deviations measured by the SWIS spectrometer and the Picaro L2140i are compared to the values expected by the volumetric propagation from mixtures preparation (Fig. 7). Data from Picarro's L2140i (both δD and $\delta^{18}O$ values) drift away from the expected value while progressively going from Sample 1 to Sample 9. The commercial instrument performs consecutives injections of the same sample, the first three are rejected because may be affected by memory effect, and the following three are averaged to obtain the final measurement (*see* Supporting Information Section-S3.2). By looking at the raw data, we could confirm that the last three measurements were not affected by memory effect. As the drift increases further away from the reference value (MQ_Fresh), this can be attributed to a nonlinearity of the instrument while moving far from the reference value. The slopes obtained by comparing the data against the expected values are 0.986 ± 0.014 (SWIS) and 0.910 ± 0.012 (Picarro) for δD measurements (Fig. 7a), and 1.02 ± 0.06 (SWIS) and

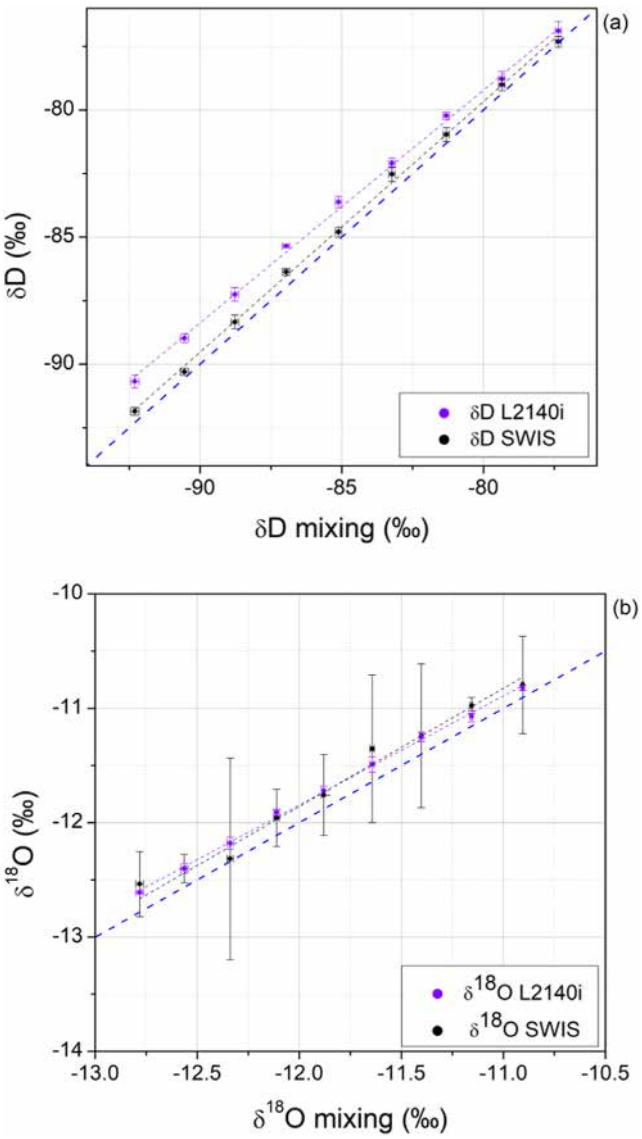

Fig. 7. Comparison of linearity between SWIS and L2140i instruments. Linear correlations were obtained with slopes of 0.986 ± 0.014 (SWIS) and 0.910 ± 0.012 (L2140i) for the δD (**a**), and 1.02 ± 0.058 (SWIS) and 0.958 ± 0.016 (L2140i) for the $\delta^{18}O$ (**b**). The blue dashed lines represent the theoretical slope values between the expected (mixing) and the measurement values.

0.958 ± 0.016 (Picarro) for $\delta^{18}O$ (Fig. 7b). For both figures, the blue dashed curve corresponds to the theoretical curve expected for the measurements from the two instruments (slope = 1). The SWIS instrument demonstrated better linearity than the Picarro instrument in the isotopic range selected for the two studied isotopologues. To compare the accuracy and precision of the two measurements, we calculated the absolute difference between the measurement and the theory (Supporting Information Section S6). In the case of δD, the SWIS instrument is more accurate with a mean deviation from theory of 0.39‰ ± 0.15‰ compared with 1.23‰ ± 0.35‰ for L2140i. For the precision, the two instruments are equivalent, with 0.22‰ on average for SWIS against 0.23‰ for Picarro at 95% confidence. Measurement of the δD isotope appears to perform better on the SWIS instrument. For $\delta^{18}O$, a similar accuracy is observed between the two instruments with an average of 0.16‰ ± 0.06‰ for SWIS against 0.15‰ ± 0.03‰ for the Picarro, but the Picarro's precision is better with an average of 0.40‰ for SWIS and 0.04‰ for Picarro at 95% confidence. The error bars obtained with the SWIS instrument are higher by a factor of 10 on average, making the measurement less accurate for this isotopologue. The Picarro instrument provides a better precision (0.04‰, 2σ), on the $\delta^{18}O$ measurement than the SWIS sensor (0.3‰, 2σ), but its accuracy would depend on how far away the isotopy of the measurement sample is from the one of the reference sample. For making accuracy close to the precision, a reference standard very close to the water to be analyzed (within 2‰ in the case of δD) is required or a non-linearity correction need to be applied to the measurement made with the commercial instrument. On the δD measurements, similar performances were achieved by the two instruments, but the SWIS instrument ensure a good linearity over the entire range studied (15‰) which is not the case for the L240i instrument. The SWIS instrument is more compact and is designed for in situ measurements, providing the high temporal and spatial resolution even in very remote and difficult to access locations (e.g., beneath an ice-shelf) and offering an easy way of deployment.

Conclusions

The instrument developed in this work offers solutions for in situ measurement of water isotopes in aquatic systems such as rivers, lakes, and oceans. Its major advantages compared with commercial instruments shown in this work are (1) an injection and sampling method adapted to in situ measurement; (2) a memory effect lower than the measurement noise within 100 s of cell cleaning; (3) the ability to perform measurement of δD, $\delta^{18}O$, and $\delta^{17}O$ simultaneously; (4) the achievement of the performances of 0.3‰ (2σ) for the three isotopologue in 9 min of measurement; (5) the dimensions in its casing (700 mm long, 165 mm internal diameter, total weight 45 kg) allowing deployment in very complex access conditions (e.g., beneath an ice shelf); (6) high hydrostatic pressure resistance allowing applications at a depth of 6000 m. Identified drawbacks and challenges are (1) the measurement in cold water (< 5°C) requires a longer measurement time and results in a low gas flow rate (< 1 sccm at maximum pumping speed); (2) external conditions in polar environments can have an impact on the instrument's temperature regulation. The SWIS sensor is unique in situ high-resolution tool for investigating the origin of water masses, and a key tool for understanding the coupling and heat exchanges between the cryosphere and the ocean, and better constraining the

principal processes responsible for the melting of the ice-shelves. Furthermore, the three isotopic signatures would allow to investigate the existence of possible mass-independent fractionations which would occurs for instance during water refreezing process. The instrument has a consumption of ~ 40 W and can be deployed with a Li-ion battery pack providing an autonomy of 10–12 h. It is designed for deployment from a ship through a borehole or on board of autonomous underwater vehicles such as AOV, ROV, and drones. It is also equipped with a SHDSL communication for telemetry propose and provide real-time data from the boat/surface. Further efforts for improving stability in the field and reduce measurement time will be performed in the future.

Data availability statement

The data are available online: https://doi.org/10.5281/zenodo.13982811.

References

Akhoudas, C., J.-B. Sallée, G. Reverdin, G. Aloisi, M. Benetti, L. Vignes, and M. Gelado. 2020. Ice shelf basal melt and Influence on dense water outflow in the southern Weddell Sea. J. Geophys. Res. Oceans **125**: e2019JC015. doi:10.1029/2019JC015710

Akhoudas, C. H., and others. 2023. Isotopic evidence for an intensified hydrological cycle in the Indian sector of the Southern Ocean. Nat. Commun. **14**: 2763. doi:10.1038/s41467-023-38425-5

Bell, R. J., R. T. Short, F. H. W. van Amerom, and R. H. Byrne. 2007. Calibration of an in situ membrane inlet mass spectrometer for measurements of dissolved gases and volatile organics in seawater. Environ. Sci. Technol. **41**: 8123–8128. doi:10.1021/es070905d

Bian, P., Y. Wang, and T. J. McCarthy. 2021. Rediscovering silicones: The anomalous water permeability of "hydrophobic" PDMS suggests nanostructure and applications in water purification and anti-icing. Macromol. Rapid Commun. **42**: 2000682. doi:10.1002/marc.202000682

Brand, W. A., H. Geilmann, E. R. Crosson, and C. W. Rella. 2009. Cavity ring-down spectroscopy versus high-temperature conversion isotope ratio mass spectrometry; a case study on δ^2H and $\delta^{18}O$ of pure water samples and alcohol/water mixtures. Rapid Commun. Mass Spectrom. **23**: 1879–1884. doi:10.1002/rcm.4083

Carter, L., I. N. McCave, and M. J. M. Williams. 2008. Chapter 4: Circulation and water masses of the Southern Ocean: A review, in: Developments in earth and environmental sciences, p. 85–114. *In* F. Florindo and M. Siegert [eds.], Antarctic climate evolution, v. **8**. Elsevier. doi:10.1016/S1571-9197(08)00004-9

Craig, H., & Gordon, L. I. (1965). Deuterium and oxygen 18 variations in the ocean and the marine atmosphere. In Tongiorgi, E. (Ed.), Stable Isotopes in Oceanographic Studies and Paleotemperatures (pp. 9–130). Consiglio Nazionale delle Ricerche, Spoleto, Italy.

Dansgaard, W. 1964. Stable isotopes in precipitation. Tellus **16**: 436–468. doi:10.1111/j.2153-3490.1964.tb00181.x

Downing, B. D., B. A. Bergamaschi, C. Kendall, T. E. C. Kraus, K. J. Dennis, J. A. Carter, and T. S. Von Dessonneck. 2016. Using continuous underway isotope measurements to map water residence time in hydrodynamically complex tidal environments. Environ. Sci. Technol. **50**: 13387–13396. doi:10.1021/acs.est.6b05745

Dupont, T. K., and R. B. Alley. 2005. Assessment of the importance of ice-shelf buttressing to ice-sheet flow, Geophys. Res. Lett. **32**: L04503, doi:10.1029/2004GL022024.

Dyroff, C., D. Fütterer, and A. Zahn. 2010. Compact diode-laser spectrometer ISOWAT for highly sensitive airborne measurements of water-isotope ratios. Appl. Phys. B **98**: 537–548. doi:10.1007/s00340-009-3775-6

Fleurbaey, H., R. Grilli, D. Mondelain, and A. Campargue. 2022. Measurements of the water vapor continuum absorption by OFCEAS at 3.50 μm and 2.32 μm. J. Quant. Spectrosc. Radiat. Transfer **278**: 108004. doi:10.1016/j.jqsrt.2021.108004

Frew, R. D., P. F. Dennis, K. J. Heywood, M. P. Meredith, and S. M. Boswell. 2000. The oxygen isotope composition of water masses in the northern North Atlantic. Deep-Sea Res. I Oceanogr. Res. Pap. **47**: 2265–2286. doi:10.1016/S0967-0637(00)00023-6

Friedman, I. 1953. Deuterium content of natural waters and other substances. Geochim. Cosmochim. Acta **4**: 89–103. doi:10.1016/0016-7037(53)90066-0

Galewsky, J., H. C. Steen-Larsen, R. D. Field, J. Worden, C. Risi, and M. Schneider. 2016. Stable isotopes in atmospheric water vapor and applications to the hydrologic cycle. Rev. Geophys. **54**: 809–865. doi:10.1002/2015RG000512

Gat, J. R. 1996. Oxygen and hydrogen isotopes in the hydrologic cycle. Annu. Rev. Earth Planet. Sci. **24**: 225–262. doi:10.1146/annurev.earth.24.1.225

Gianfrani, L., G. Gagliardi, M. van Burgel, and E. R. T. Kerstel. 2003. Isotope analysis of water by means of near-infrared dual-wavelength diode laser spectroscopy. Opt. Express **11**: 1566–1576. doi:10.1364/OE.11.001566

Golledge, N. R., E. D. Keller, N. Gomez, K. A. Naughten, J. Bernales, L. D. Trusel, and T. L. Edwards. 2019. Global environmental consequences of twenty-first-century ice-sheet melt. Nature **566**: 65–72. doi:10.1038/s41586-019-0889-9

Gordon, I. E., and others. 2017. The HITRAN2016 molecular spectroscopic database. J. Quant. Spectrosc. Radiat. Transfer **203**: 3–69. doi:10.1016/j.jqsrt.2017.06.038

Grilli, R., and others. 2018. Sub-ocean: Subsea dissolved methane measurements using an embedded laser spectrometer technology. Environ. Sci. Technol. **52**: 10543–10551. doi:10.1021/acs.est.7b06171

Grilli, R., T. DelSontro, J. Garnier, F. Jacob, and J. Némery. 2023. A novel high-resolution in situ tool for studying carbon

biogeochemical processes in aquatic systems: The Lake Aiguebelette case study. Journal of Geophysical Research: Biogeosci. **128**: e2022JG007200. doi:10.1029/2022JG007200

Gruber, N., P. Landschützer, and N. S. Lovenduski. 2019. The variable Southern Ocean carbon sink. Ann. Rev. Mar. Sci. **11**: 159–186. doi:10.1146/annurev-marine-121916-063407

Gupta, P., D. Noone, J. Galewsky, C. Sweeney, and B. H. Vaughn. 2009. Demonstration of high-precision continuous measurements of water vapor isotopologues in laboratory and remote field deployments using wavelength-scanned cavity ring-down spectroscopy (WS-CRDS) technology. Rapid Commun. Mass Spectrom. **23**: 2534–2542. doi:10.1002/rcm.4100

Haumann, F. A., N. Gruber, M. Münnich, I. Frenger, and S. Kern. 2016. Sea-ice transport driving Southern Ocean salinity and its recent trends. Nature **537**: 89–92. doi:10.1038/nature19101

Hoch, G., and B. Kok. 1963. A mass spectrometer inlet system for sampling gases dissolved in liquid phases. Arch. Biochem. Biophys. **101**: 160–170. doi:10.1016/0003-9861(63)90546-0

Johnson, R. C., R. G. Cooks, T. M. Allen, M. E. Cisper, and P. H. Hemberger. 2000. Membrane introduction mass spectrometry: Trends and applications. Mass Spectrom. Rev. **19**: 1–37. doi:10.1002/(SICI)1098-2787(2000)19:1<1::AID-MAS1>3.0.CO;2-Y

Kerstel, E. 2004. Chapter 34: Isotope ratio infrared spectrometry, p. 759–787. *In* P. A. de Groot [ed.], Handbook of stable isotope analytical techniques. Elsevier. doi:10.1016/B978-044451114-0/50036-3

Kerstel, E. R. T., G. Gagliardi, L. Gianfrani, H. A. J. Meijer, R. van Trigt, and R. Ramaker. 2002. Determination of the $^{2}H/^{1}H$, $^{17}O/^{16}O$, and $^{18}O/^{16}O$ isotope ratios in water by means of tunable diode laser spectroscopy at 1.39 μm. Spectrochim. Acta A Mol. Biomol. Spectrosc. **58**: 2389–2396. doi:10.1016/S1386-1425(02)00053-7

Kerstel, E. R. T., R. Iannone, M. Chenevier, S. Kassi, H.-J. Jost, and D. Romanini. 2006. A water isotope (^{2}H, ^{17}O, and ^{18}O) spectrometer based on optical feedback cavity-enhanced absorption for in situ airborne applications. Appl. Phys. B **85**: 397–406. doi:10.1007/s00340-006-2356-1

Landsberg, J., D. Romanini, and E. Kerstel. 2014. Very high finesse optical-feedback cavity-enhanced absorption spectrometer for low concentration water vapor isotope analyses. Opt. Lett. **39**: 1795–1798. doi:10.1364/OL.39.001795

Lechevallier, L., S. Vasilchenko, R. Grilli, D. Mondelain, D. Romanini, and A. Campargue. 2018. The water vapour self-continuum absorption in the infrared atmospheric windows: New laser measurements near 3.3 and 2.0 μm. Atmos. Meas. Tech. **11**: 2159–2171. doi:10.5194/amt-11-2159-2018

Lechevallier, L., R. Grilli, E. Kerstel, D. Romanini, and J. Chappellaz. 2019. Simultaneous detection of C_2H_6, CH_4, and δ^{13}C-CH4 using optical feedback cavity-enhanced absorption spectroscopy in the mid-infrared region: Towards application for dissolved gas measurements. Atmos. Meas. Tech. **12**: 3101–3109. doi:10.5194/amt-12-3101-2019

Majoube, M. 1971. Fractionnement en oxygène 18 et en deutérium entre l'eau et sa vapeur. J. Chim. Phys. **68**: 1423–1436. doi:10.1051/jcp/1971681423

Millan, R., E. Jager, J. Mouginot, M. H. Wood, S. H. Larsen, P. Mathiot, N. C. Jourdain, and A. Bjørk. 2023. Rapid disintegration and weakening of ice shelves in North Greenland. Nat. Commun. **14**: 6914. doi:10.1038/s41467-023-42198-2

Morville, J., S. Kassi, M. Chenevier, and D. Romanini. 2005. Fast, low-noise, mode-by-mode, cavity-enhanced absorption spectroscopy by diode-laser self-locking. Appl. Phys. B **80**: 1027–1038. doi:10.1007/s00340-005-1828-z

Morville, J., D. Romanini, and E. Kerstel. 2014. Cavity enhanced absorption spectroscopy with optical feedback, p. 163–209. *In* G. Gagliardi and H.-P. Loock [eds.], Springer series in optical sciencesCavity-enhanced spectroscopy and sensing. Springer. doi:10.1007/978-3-642-40003-2_5

Nelson, S. T. 2000. A simple, practical methodology for routine VSMOW/SLAP normalization of water samples analyzed by continuous flow methods. Rapid Commun. Mass Spectrom. **14**: 1044–1046. doi:10.1002/1097-0231(20000630)14:12<1044::AID-RCM987>3.0.CO;2-3

Olsen, J., I. Seierstad, B. Vinther, S. Johnsen, and J. Heinemeier. 2006. Memory effect in deuterium analysis by continuous flow isotope ratio measurement. Int. J. Mass Spectrom. **254**: 44–52. doi:10.1016/j.ijms.2006.05.004

Padman, L., M. R. Siegfried, and H. A. Fricker. 2018. Ocean tide influences on the Antarctic and Greenland ice sheets. Rev. Geophys. **56**: 142–184. doi:10.1002/2016RG000546

Penna, D., and others. 2012. Technical note: Evaluation of between-sample memory effects in the analysis of $\delta^{2}H$ and $\delta^{18}O$ of water samples measured by laser spectroscopes. Hydrol. Earth Syst. Sci. **16**: 3925–3933. doi:10.5194/hess-16-3925-2012

Polyakov, I. V., and others. 2017. Greater role for Atlantic inflows on sea-ice loss in the Eurasian Basin of the Arctic Ocean. Science **356**: 285–291. doi:10.1126/science.aai8204

Pritchard, H. D., S. R. M. Ligtenberg, H. A. Fricker, D. G. Vaughan, M. R. Van Den Broeke, and L. Padman. 2012. Antarctic ice-sheet loss driven by basal melting of ice shelves. Nature **484**: 502–505. doi:10.1038/nature10968

Richard, L., D. Romanini, and I. Ventrillard. 2018. Nitric oxide analysis down to ppt levels by optical-feedback cavity-enhanced absorption spectroscopy. Sensors **18**: 1997. doi:10.3390/s18071997

Sallée, J.-B., V. Pellichero, C. Akhoudas, E. Pauthenet, L. Vignes, S. Schmidtko, A. N. Garabato, P. Sutherland, and M. Kuusela. 2021. Summertime increases in upper-ocean stratification and mixed-layer depth. Nature **591**: 592–598. doi:10.1038/s41586-021-03303-x

Sayres, D. S., and others. 2009. A new cavity based absorption instrument for detection of water isotopologues in the

upper troposphere and lower stratosphere. Rev. Sci. Instrum. **80**: 044102. doi:10.1063/1.3117349

Schloesser, F., T. Friedrich, A. Timmermann, R. M. DeConto, and D. Pollard. 2019. Antarctic iceberg impacts on future Southern Hemisphere climate. Nat. Clim. Change **9**: 672–677. doi:10.1038/s41558-019-0546-1

Schlosser, P. 1986. Helium: A new tracer in Antarctic oceanography. Nature **321**: 233–235. doi:10.1038/321233a0

Serreze, M. C., and R. G. Barry. 2011. Processes and impacts of Arctic amplification: A research synthesis. Global Planet. Change **77**: 85–96. doi:10.1016/j.gloplacha.2011.03.004

Swart, N. C., S. T. Gille, J. C. Fyfe, and N. P. Gillett. 2018. Recent Southern Ocean warming and freshening driven by greenhouse gas emissions and ozone depletion. Nat. Geosci. **11**: 836–841. doi:10.1038/s41561-018-0226-1

Ventrillard-Courtillot, I., T. Gonthiez, C. Clerici, and D. Romanini. 2009. Multispecies breath analysis faster than a single respiratory cycle by optical-feedback cavity-enhanced absorption spectroscopy. J. Biomed. Opt. **14**: 064026. doi:10.1117/1.3269677

Walker, S. A., and others. 2016. Oxygen isotope measurements of seawater (H_2 $^{18}O/^{16}O$): A comparison of cavity ring-down spectroscopy (CRDS) and isotope ratio mass spectrometry (IRMS). Limnol. Oceanogr. Methods **14**: 31–38. doi:10.1002/lom3.10067

Werle, P., R. Mücke, and F. Slemr. 1993. The limits of signal averaging in atmospheric trace-gas monitoring by tunable diode-laser absorption spectroscopy (TDLAS). Appl. Phys. B **57**: 131–139. doi:10.1007/BF00425997

Wijmans, J. G., and R. W. Baker. 1995. The solution-diffusion model: A review. J. Membr. Sci. **107**: 1–21. doi:10.1016/0376-7388(95)00102-I

Acknowledgments

The authors would like to thank the technical service at IGE laboratory, and particularly Philippe Possenti, Romain Duphil, Eric Lefebvre, and Luc Piard, for their technical help on this development, the LSCE laboratory for providing the IRMS measurements of the reference standard waters used in this study, the colleagues from LOCEAN, Claire Waelbroeck, Gilles Reverdin, and Jean-Baptiste Sallée for the fruitful discussions on the futures applications of the instrument. Nicolas Jourdain, Roberto Grilli, and Julien Witwicky were supported by the EU, Horizon Europe Funding Programme for research and innovation. This study was funded by the Agence Nationale de la Recherche (ANR) under grant agreement ANR-18-CE04-0003-01 (SWIS), "Investment for Future - Excellency Equipment" project TERRA FORMA with the reference ANR-21-ESRE-0014 and by the European Union, Horizon Europe Funding Programme for research and innovation under grant agreement Nr. 101060452 (OCEAN:ICE).

Conflict of Interest

None declared.

Submitted 18 June 2024
Revised 30 October 2024
Accepted 08 November 2024

Associate editor: Isaac Santos